THE EFFECT OF CROSS-SECTION GEOMETRY ON CRUSHING BEHAVIOUR OF 3D PRINTED CONTINUOUS CARBON FIBRE REINFORCED POLYAMIDE PROFILES

U. Morales (*), A. Esnaola, M. Iragi, L. Aretxabaleta and J. Aurrekoetxea

Mechanical and Industrial Production Department,
Mondragon Unibertsitatea, Loramendi 4, 20500 Mondragón, Spain
Corresponding Author (*) Email: umorales@mondragon.edu, Web Page: http://www. mondragon.edu

Abstract

The present study has analysed the effect of cross-section geometry and the printing pattern of continuous carbon reinforced polyamide on the axial and radial crushing behaviour. Each geometry and printing pattern generated singular defects, but the most relevant microstructural aspect resulted the fibre orientation. The geometry with the re-entrant shape and Concentrical printing pattern was identified as the best profile for axial and radial crushing loadings, with a *SEA* of 23.9 and 5.9 kJ/kg. In spite of axial *SEA* values are far from those values obtained for composite profile manufactured by conventional process, radial *SEA* value obtained with steered fibres was at least 2-3 times higher than the best value found in the literature. Thus, concentrically 3D printed with steered fibres layers, could be exploited for radially loaded hollow profiles applications. Despite studied cross-section are not good enough under axial loads, 3D printing allows complex geometries and exploring more sophisticated cross-sections could lead to higher axial *SEA* values.

Keywords: *SEA*, crush, 3D printing, continuous carbon fibre composite, hollow profile.

Highlight

- The best 3D printed profile achived an axial and radial *SEA* of 23.9 and 5.9 kJ/kg, respectively.
- The re-entrant shape of the profile induced the stable collapse.
- The performance of profiles with steered fibres were higher than those with longitudinal straight-fibres.

1. Introduction

Fuel efficiency and passenger safety are the two main drivers of the present day vehicle manufacturing sector. Continuous fibre reinforced plastic (FRP) composites combined with complex designs for safe and lightweight primary structures are increasingly being employed to meet these challenges [1]. FRPs are widely studied in terms of specific stiffness, strength and impact energy absorption, and show 3-10 times higher specific energy absorption (*SEA*) than metallic alloys [1,2]. For this reason, FRP structures are integrated in the body-in-white of vehicles and aircraft fuselage for crashworthiness applications such as crash-box [3,4] or cabin subfloor vertical struts [5].

From the design point of view, most crashworthiness components are thin-walled spaceframes, since these profiles are able to dissipate a high-energy in impact scenarios [6]. Several authors [7-12] have reported that the main parameters affecting *SEA* of composite structures are the profile transverse section, the design and location of triggers, the reinforcement architecture, the fibre orientation, as well as the fibre and void content.

Interest in fibre reinforced thermoplastics (FRTP) has increased in recent years as their toughness and elongation at breakage are higher than those of thermosets [11,13]. Different conventional manufacturing processes have been explored for car body components, such as compression moulding

[11], thermoforming [14], filament winding, automatic tape layup [15] or automatic fibre placement [16], but their restrictions in terms of complex design, non-conventional fibre orientation or costs, limit the usage of FRTP.

Additive manufacturing, and namely Filament Fused Fabrication (FFF), become a key enabling technology for developing highly customised products. This manufacturing process permits the use of advanced materials (steered-fibres, dispersed stacking sequence laminates or functionally graded composites) in combination with complex geometries (lattice, cellular or auxetic structures) to satisfy the demand for lightweight design concepts in the transportation industry.

There are two approaches for FFF of continuous fibre reinforced composites [17-19]. The first, in-nozzle impregnation, has been applied to non-engineering polymers such as acrylonitrile butadiene styrene (ABS) [20] and polylactic acid (PLA) [21], and the resulting composites have shown impregnation and compaction problems that limited their mechanical properties. The second technology for printing continuous FRTP uses a pre-impregnated filament, and thus impregnation problems are prevented [17,18]. Polyamide matrix (PA) has been successfully applied to 3D printed continuous carbon fibre reinforced plastic (CF-PA) using FFF techniques [22-30]. The mechanical properties characterisation of printed CF-PA has been carried out by several authors following standard testing methods such as tensile [22,24,28-30], compression [24,27], bending [23,27,29], in-plane shear [24,28], interlaminar strength [23,25,28], quasi-static indentation [23], interlaminar fracture (Mode I and Mode II) [28] and impact [26]. Three main conclusions can be drawn from these studies: (i) the existence of an interlayer with high void-content reduces the mechanical properties of the printed CF-PA, (ii) there is difference between the nozzle path/trajectory and the resulting orientation of the printed fibre, and (iii) both are due to the nature of the FFF printing (layer-by-layer) process. However, no studies investigating the complex geometry or the complex loading of printed CF-PA have been found**.**

As regards geometry, only few studies [23,30] have reported the influence of the part geometry and printing path on fibre-placement defects. The energy dissipation of 3D printed structures under crushing or bending loads have been studies, [31-37] however the reported lattice structures are based on honeycomb or auxetic concepts manufactured by FFF of unreinforced plastics, e.g. PLA [31], ABS [32] or TPU (thermoplastic polyurethane) [33]. Only four papers have been found which analyse continuous carbon sandwich structures under crushing. In these works, these approaches were explored: fully 3D printed parts [34,35], and 3D printed cores with conventional composite skins [36,37].

The present paper analyses the crushing behaviour of 3D printed thin-walled hollow structures composed of complex continuous fibre orientations, a combination that, to the knowledge of the authors, has not been studied to date. No studies related to the collapse mode of a printed profile under crushing have been found in the literature, and furthermore, there is limited information available regarding the fracture mechanisms which induce stable crushing behaviour and enhance the crashworthiness of vehicles. The objective of this study is to characterise the crushing behaviour and specific energy absorption (*SEA*) capability of continuous carbon fibre reinforced polyamide thin-walled hollow profiles manufactured by FFF. To this end, two cross-section geometries, longitudinal and concentric fibre orientations, as well as axial and radial quasi-static crushing were analysed. The collapse mode and fracture micromechanisms were also investigated, so as to better understand the effect of the aforementioned parameters.

2. Experimental procedures

2.1. Materials

A Mark Two® 3D printer from Markforged was employed for the production of the specimens. The printed composite material was a continuous carbon fibre reinforced polyamide (CF-PA) and the infill material used was a polyamide 6 reinforced with carbon micro-fibres (Onyx®). Both materials are commercial grades from Markforged and their density and mechanical properties are reported in Table 1.

{Insert Table 1}

2.2. Specimens design and 3D printing process

The two profile designs are shown in Figure 1, and their geometrical properties are summarized in Table 2. The Fold (Figure 1a) was based on the transverse sections with radial corrugation studied by Belingardi *et al*. [7], whereas the second one was a hexagonal profile (Figure 1b) used when axial crushing is the dominant loading case [3,9,10]. The compression specimens were 60 mm in length and 3 mm in thickness profiles. The criterion established to compare the results of both profiles was to equalise the cross-section areas and moments of inertia about y-axis.

{Insert Figure 1}

{Insert Table 2}

Based on the STL file, Eiger® software can generate two different printing patterns for continuous fibre reinforced filaments: concentric and isotropic. In the concentric approach, the printing head follows the outer profile of the part and places a single strand of fibre inwards in rings from that outer boundary. The second option is the isotropic, where the fibre orientation is independent of the cross-section geometry and the fibres are deposited in straight lines following a fixed orientation defined by the user for each layer. In both cases, the starting point is a potential area of weakness, so in each layer Eiger® automatically moves this starting point around the part, generating a good overlap. The samples printed with the main axis (x-axis) parallel to the printing bed had an isotropic printing pattern (hereinafter referred to as Longitudinal), whereas the concentric strategy was used for samples with the main axis perpendicular to the bed, (identified as Concentric). For all the specimens, the filling density was 100% and only one contour wall of Onyx® was used in order to maximize the fibre content. The extrusion and filling parameters used to print the specimens are shown in Table 2.

{Insert Table 3}

The name codification of the specimens is as follows; the first capital letter is referred to the profile's geometry (F for Fold and H for Hexagonal), the second one identifies the printing pattern (L for Longitudinal and C for Concentric), and the third identifies the loading case (A for Axial and R for Radial).

2.3. Microstructure and fracture surface inspection

The microstructure, fibre distribution and voids of the printed specimen were characterized using optical microscopy (OLYMPUS-GX51). The samples have been prepared by the following procedure: the samples were cut perpendicular (transverse view) or parallel (longitudinal view) to the main axis, ground using 600 grit SiC paper and then polished with a 1 µm monocrystalline diamond suspension on polishing cloth. Failure modes were studied by analysing the fracture zones of printed profile with an optical macroscopy (Leica DMS 1000).

2.4. Compression tests

Before testing, the specimens were conditioned for 48 hours at 23 ºC and 55% RH. Quasi-static compression tests were carried out using a Hoyton/HM-D universal testing machine equipped with a 100 kN load cell. The overall displacement was registered from the encoder of the ball-screw. The crosshead speed was 10 mm/min along the collapse distance l, and the tests were carried out at room temperature and 55% RH. The specific energy absorption SEA (kJ/kg); mean load P_{mean} (kN), maximum load P_{max} (kN), load uniformity LU (-) and stroke efficiency SE (-), were calculated from the registered force-displacement curves by the following equations:

$$SEA = \frac{\int_0^{l_{max}} P(l)dl}{m_t} \quad (1)$$

$$P_{mean} = \frac{\int_0^{l_{max}} P(l)dl}{l_{max}} \quad (2)$$

$$LU = \frac{P_{mean}}{P_{max}} \quad (3)$$

$$SE = \frac{l_{max}}{H} \quad (4)$$

where, l_{max} (mm) is the total collapsed length, m_t is the crushed specimen mass (kg) and H specimen height (mm). The total collapsed length corresponds to the maximum displacement reached during the crushing test. It is necessary to run the compression test until material densification or separation, which is the moment when a significant profile stiffness change occurs.

3. Results and discussion

3.1. Microstructure analysis

This section discusses the effect of the printing parameters on the microstructures of the composites. The interlayer bonding has been determined as the most important factor on the mechanical properties and performance of printed material [17,18]. In fact, different adherence of layers has been shown to lead to different fracture patterns, crack growth and hence may affect to the energy absorption capability of printed composites [30]. In Mark Two® 3D printer processing parameters, such layer thickness and interbead spacing, are fixed by Eiger© and therefore the pressure applied is not controlled.

The transverse and longitudinal section of Longitudinal and Concentric samples are shown in Figure 2. The microstructure at the contour wall ring of Onyx® showed a well dispersed carbon short-fibres (Figure 2a). Additionally, no evidences of printing tracks were reported, but voids between beads could be appreciated (Figure 2b). In fact, the inclusion of carbon chopped fibre has shown to not only improve the mechanical properties of printed samples but also enhance the heat transfer between printed tracks, leading to improved bonding [23,30].

The cross-section perpendicular to the printing path for the continuous fibre reinforced composites is shown in Figures 2c and 2d. Although the initial filament was cylindrical, in the Longitudinal samples the resulting geometry was a flattened layer. This was because a compression load was applied during the printing process and a partial overlapping existed between adjacent filaments. It can be also observed that the thickness and width of the different layers were regular. Good bonding between the Onyx© contour wall and inner continuous fibre beads was observed through overlapping Onyx© and prepreg filaments (Figure 2c). The non-homogeneous fibre bundles distribution and resin-rich zones likely have their origin in the initial filament microstructure, as reported by Blok *et al.* [30].

Regarding the interlayer bonding quality, unlike in the Onyx® case, the printing tracks were visible. Additionally, higher void-content in the interface than Onyx® is also observed. These defects are related to the low temperature and pressure inherent to FFF during the whole cicatrisation process [26].

The interbead voids were not spherical as can be seen in the transverse sections (Figures 2c and 2d). Moreover, they were founded to be longer than 10 times the width of the printed bead (1 mm) as it is observed in the longitudinal view (Figure 2e), and previously reported by Goh *et al.* [23]. Even when the printing path was straight, layered beads presented undulations, generating the aforementioned

interbead voids and fibre undulations [26,35]. In the concentric samples, for straight printing paths, the same microstructural features were been found between the fibres rings (Figure 2f).

{Insert Figure 2}
Color should be used for Figure 2 in print

3.2. Fibre placement analysis

The influence of profile geometry and printing pattern on fibre-placement defects at singular locations such as corners, radii and edges of the profiles are analysed in this section. These singular points are of special interests since they correspond to stress concentration areas for crack and failure initiation [7], and thus the presence of defects in these locations can increase the risk of premature failure of the structure. In accordance with to previous studies [23,30,35,39], the fibre-placement defects were analysed and classified, resulting in a defect-map for each samples profile (Figure 3).

{Insert Figure 3}

Figures 4a-c show the defects inherent in the samples with Longitudinal fibre orientation. In bent regions, due to the layered nature of FFF parts and to the fact that the beads were flattened, caused a staggered structure to be built up. As a consequence a non-homogeneous fibre volume content was generated along the perimeter of the two Longitudinal profiles (Figure 4a). This defect is particularly prominent in sharp transition zones, where Eiger© has difficulties for placing fibres and tries to fill the gap with Onyx®. Unfortunately, the filling and compaction quality at these regions was not satisfactory, and this lack of material lack persisted in both printing pattern (Figure 4b and c).
In the samples printed with Concentrical patterns (Figures 4d-f), it is important to note that printing follows a spiral path starting at the outside contour and finishes inward [30]. This motion induces fibres undulations [35], and generates interbead voids as can be observed in Figure 4d. Moreover, evidence of fibre twisting and folding back have been reported in zones of reduced turning radius in the two profiles. Fibre twisting is related to the restricted rotation of the extrusion head during a curved path, and it has been found that a minimum critical radius exists for each fibre bundle size [35,39]. For radii from 1 to 3mm both defects were detected (Figure 4e), whereas solely fibre twisting (Figure 4f) was observed in radii larger than 3 mm. Finally, even for the smallest turning radius, no evidence of carbon fibre breakage was found, contrary to the findings of Goh *et al.* [23].

{Insert Figure 4}
Color should be used for Figure 4 in print

To complete the study, the microstructure was analysed at a macroscale level and a discrepancy between the designed profile thickness and the manufacturing effective thickness can be observed. Although the profiles were designed with a constant wall thickness of 3 mm, in the additive manufacturing process, the thickness is determined by the slicing of the part in parallel planes to the printing bed, and consequently the thickness varies on the Longitudinal samples depending of the angle at each zone.
The second aspect to consider is that the printed beads had a flattened shape and and their width was greater than their height. Continuous fibre reinforced beads are 0.18 mm in height and 1 mm in width [23], whereas Onyx® beads have a height of 0.125 mm and a width of 0.595 mm (Figure 5a). When the sliced thickness is not an integer multiple of the combination of Onyx® and fibre reinforeced beads widths, a lack of material occurs. Furthermore, Eiger® determines the number of Onyx® and fibre reinforced beads that best fills the sliced thickness. Consequently, different contour thicknesses and fibre content were found in each layer (Figure 5b). The fibre content differences were even higher when walls of the same thickness were printed horizontally and vertically. In horizontal walls, the thickness of the contour wall is determined by the Onyx® bead height, whereas in vertical walls the

contour thickness corresponds to the width of Onyx®. As a result, a higher fibre volume content was founded in horizontal walls (Figure 5c).

{Insert Figure 5}
Color should be used for Figure 5 in print

3.3. Compression test

3.3.1. Axial crushing pattern

The axial crushing pattern of the two geometries and two fibre orientations are shown in Figure 6. The crush behaviour of FRP profiles during axial compresion are classified as progressive (stable) or catastrophic (unstable). The general axial crushing behaviour of the both geometries might be divided in two stages: the first stage is driven by the elastic response of the material, whereas the second stage is governed by the material plasticity and fracture toughness. The crushing curves of both failure modes presented common features at the first stage: an initial elastic zone (point 1) until the first peak load is reached (point 2), then crushing collapse begins and load drops (point 3). The crushing curves for the samples with catastrophic failure finish at this point, whereas those with progressive collapse continues under a constant load (point 4). Finally, the densification of the sample due to section folding induces the load to rise (point 5). Figure 6 additionally shows representative pictures of the samples in each of the crushing stages. The crushing pattern of each sample is described in the following paragraphs.

The FLA specimen underwent a catastrophic failure after peak load was reached (point 2´) whereas FCA sample has presented a stable crushing mode driven by a pseudo-ductile (point 2) failure mechanism of progressive folding. The initial FLA fracture was located at the contact zone between the plate and specimen, involving short-length fracture (fragmentation) of fibres and followed by profile axial splitting. Then, longitudinal crack propagation grew rapidly and the specimen failed into a brittle manner. Crack propagation occurred parallel to the printed interface and it was controlled by the interlayer delamination fracture mechanism.

The FCA specimen presented the longest crushing length with a large nearly plateau stage (point 4), followed by a secondary peak load (point 5), which is due to material densification when section folding occurred. The presence of concentrically oriented continuous fibres influenced directly in the longitudinal crack propagation, failure mechanism and therefore in the energy absorption capability of the printed profile [6,12,40].

In the case of HLA, this sample underwent an unstable collapse mode similar to the FLA, and with comparable performance in terms of energy absorption capacity. Following a similar trend to the FCA, the HCA sample showed a stable collapse with a long constant-load stage (point 4), followed by secondary peak load due to material densification (point 5). Nevertheless, the amount of energy absorbed by HCA was slightly lower than the FCA.

On the one hand, according to the *SEA* values set out in Table 4, the Concentric specimens exhibited enhanced energy absorption properties due to their longer collapse lengths. In fact, the highest *SEA* value (23.9 kJ/kg) corresponding to the FCA sample and was double of the highest value of the Longitudinal samples. Addittionally, the Concentric samples showed the lowest peak value (22.2 kN for FCA), which is a favourable from the crushing point of view. However, the axial stiffnesses calculated as the initial slope of the curve (point 1´) were higher for Longitudinal samples, with a average value of 14.8 kN/mm.

The first significant finding was that similar crushing curves were observed (Figure 6) when the geometry of the profiles changed, since the transverse area and inertia (I_{yy}) of the profiles were similar (Table 2). It can therefore be concluded that the axial crushing pattern of the studied profiles is more dependant on material than on geometry.

{Insert Figure 6}
Color should be used for Figure 6 in print

{Insert Table 4}

3.3.2. Radial crushing pattern

The radial crushing behaviours of the two hollow profiles and two fibre orientations are shown in Figure 7. Their typical radial progressive crushing patterns are divided in three stages; the first stage is driven by linear elasticity (point 1) until the first hinges are generated in singular points of the transverse section (point 2), such as corners, thickness changes or corrugations. These points have been identified by other authors as stress concentration zones and crack tips initiators for progressive tearing lines in the longitudinal direction [7]. In the second stage, the crushing mechanism continues and the transverse section geometry suffers significant changes (point 3), developing larger deformed zones at the singular points. In the final stage, the load increases gradually as the amount of collapse hinges increases (point 4) and the inner walls of the sections make contact (point 5 and 6).

The FLR presented an unstable collapse mode with sharp load peaks due to a brittle fracture of the material at points 1´, 2´ and 3´. These points corresponded to the formation of longitudinal cracks at the upper corner, mid-span and section's corrugation before a snap drop of load occurred. The resulting tear lines formed folds which resulted in significant changes in the profile cross section. After hinges formed in the corrugation zone, the load become nearly constant (plateau) until the corrugation faces made contact. Then, the load increased due to the material densification (point 4´). Once the upper part of the section collapsed, additional hinges developed at the bottom corner and promoted the full folding of the profile (point 5´). Finally, the load rose exponentially (point 6´).

The FCR in contrast, exhibited a pseudo-ductile response, with a spring-back effect during the unloading path. No material plastification, neither sharp peaks, were observed during hinges formation. Due to the fact that FCR corners have been reinforced by continuous carbon fibres, higher loads were reached and higher energy was also absorbed during FCR crushing.

The HLR showed a non-progressive collapse behaviour once the longitudinal cracks were initiated, firstly at mid-height (point 2´) and then at the upper and bottom edges (point 3´). The post-buckling stiffness became negligible due to the location of the hinges, and radial loading was no longer supported, inducing a sudden fail of the section. Insofar as the crushing behaviour was unstable, the energy absorption was also low. Furthermore, an unstable crush failure mode was observed in the HCR sample, resulting in a low *SEA* value. In spite of pseudo-ductile failure and plastic hinge generation, once the first hinges at the centre edge of the hexagon (point 2) yielded, and two more were developed (point 3) at the upper and bottom edges (point 4), the section was rendered unstable.

According to the *SEA* values set out in Table 5, the highest values were obtained for the Concentric configuration. The Fold profile, and namely FCR, delivered the best energy absorption performance under radial loading with a *SEA* value of 5.9 kJ/kg, whereas HCR only absorbed 1.6 kJ/kg.

Moreover the FCR sample exhibited the highest maximum load and radial stiffness, reaching a maximum load of 15.8 kN. In this respect, the radial stiffness of FCR calculated at point 1 was about 4.8 kN/mm (4 times less than axial stiffness).

Similarities were found between collapse curves (Figure 7) of samples with Longitudinal and Concentric printing patterns, since both materials allowed the formation of hinge-like areas at the transverse section corners, driving the progressive failure of the profiles. These hinge-like formations (location and sequence) and their progress were identified as a driver of stable collapse during the crushing process. Hence, it can be concluded that the radial crushing pattern behaviour of the studied profiles is more dependant on geometry than on material.

{Insert Figure 7}

Color should be used for Figure 7 in print

{Insert Table 5}

3.4. Fracture surface inspection

The failure patterns described in the previous sections are completed with the analysis of the fracture micromechanism at the failure points.

3.4.1. Axial compression test.

The weak interlayer surfaces of the Longitudinal samples were oriented parallel to the load direction. Consequently, axial cracks were generated through interbead surfaces by matrix and matrix-fibre fracture. Once the samples were cracked, energy was absorbed by the bending of independent bundles of fibres and lamina as well as by fibre breaking (Figure 8a). In the contact zone between Longitudinal specimens and test plates, where barrelling was induced, evidence of fibre buckling was indicated by the presence of kink-bands (Figure 8b), similar observation were found in Goh *et al.* and Iragi *et al.* studies [23,28].
In the case of the Concentric samples, the weak interlayer surfaces were compressed, preventing Mode I crack propagation. Fibre splaying failure mechanism and fibre breakage were also observed during folding for the both profiles, promoting finite fibre debonding and slippage to absorb the energy. Evidence of fibre pull-out during carbon fibre ring expansion were also found (Figure 8c), which might denotes the aforementioned matrix-fibre failure (Figure 8d), maybe due to improper impregnation [22,24]. However, signs of fibre bridging were found in postbuckling Concentric samples (Figure 8e), which supports the hypothesis that fibre impregnation is quite high.

3.4.2. Radial compression test.

The tests revealed evidence of two different kind fracture mechanism generating hinge-points. Both were based on interlaminar shear failure and allowed stable crushing of the profile (Figure 8f and Figure 8g). The first occurred at interlayers of the Longitudinal samples (Figure 8f), and its fast growth implied a sudden drop on the profile stability, with a consequent low rate of energy absorption. The second occurred in the interbeads of the Concentric samples (Figure 8g). Interbead friction contributed to a slow crack-growth mechanism, which allowed continuous absorption of energy without affecting the stability of the profile.

{Insert Figure 8}
Color should be used for Figure 8 in print

3.5. Discussion of results

In section 3.3 the results has been discussed in term of loading cases. In this section, the behaviour on the both loading direction will be analysed. The crush behaviour of the tests performed are summarised in Table 6. Among all samples studied, the Concentric samples were the only presenting a stable crush mode under axial loading, since the interlayer was loaded to compression. On the other hand, in radial load case, only the Fold samples exhibited a progressive failure mode independently of the fibre printing strategy. The reentrant geometry of the Fold profile ensured this stable collapse during radial loading.

{Insert Table 6}

The energy absorption capabilities of the profiles subjected to axial loading were higher than those obtained in radial loading because the lateral stiffness of the profiles were limited [39]. In both loading cases, the combination of the Fold profile and the Concentric configuration exhibited the best *SEA* values, being 23.9 kJ/kg, in axial and 5.9 kJ/kg in radial loading.
The axial absorption capabilities achieved in this research were far from the *SEA* values (Table 7) obtained for the conventional manufacturing process of composite. The difference in this results, could be attributed to the fact that printed composites have a lower fibre volume content (max. 30%) and higher void volume content (min. 7%) [29].

{Insert Table 7}

Nevertheless, with printed samples a four times higher *SEA* value was achieved for radial loading (Table 8). By adding concentrical continuous carbon filament composites (steered fibre), as the fibres provide local reinforcement at singular points identified in Figure 3, crushing performance was enhaced.

{Insert Table 8}

4. Conclusions

The present study has analysed the effect of cross-section geometry and the printing pattern of continuous carbon reinforced polyamide on the axial and radial crushing behaviour. From the microstructure analysis, the main defect in the Longitudinal samples was the difference in contour thickness from layer to layer, which generates a heterogeneous fibre content at layer level. Additionally, in the layers where the thickness is not an integer multiple of the beads' width, a lack of material is found at the interface between the contour wall and the inner zone. In the samples with Concentric fibre configuration, fibre twisting and folding back were found for radii smaller than 3 mm, but above only twisting appeared. Undulation of fibre bead were reported in Longitudinal and Concentric samples. However, the interbead void defects were magnified at Concentric due to steered fibres.

Under axial crushing conditions, the geometry with the re-entrant shape's performance was better than the hexagonal. Concentric specimen doubled the *SEA* of Longitudinal specimen, with a lower peak force and stable collapse, which is beneficial for energy absorbing structures. However, the axial stiffness of Concentric samples was lower. These differences could be justified by the fibre orientations, that promoted different fracture micromechanisms; in Longitudinal samples axial cracks were generated through interlayer surfaces, whereas in the Concentric samples interlayer surfaces subjected compression load and the weak points were the interbeads, inducing fibre splaying and fibre breakage. The maximum *SEA*, 23.9 kJ/kg, obtained with printed samples was far from the values of composites profiles obtained with conventional manufacturing process. The lower fibre content in 3D printed composites could be the main reason for their lower axial properties.

The results for radial crushing tests also demonstrated that re-entrant geometry was better than the Hexagonal, and the samples with Concentric printing pattern exhibited higher *SEA* values. The steered fibres provide local reinforcement at singular points where stress concentration is located, resulting in a better crushing performance. In spite of fibre volume content of printed profiles being lower that the one of composite profiles manufactured with conventional technologies, the *SEA* obtained with steered fibres (5.9 kJ/kg) was at least 2-3 times higher than the best value found in the literature.

In conclusion, concentrically 3D profiles printed with steered fibres layers, unfeasible for conventional manufacturing processes, could be exploited for radially loaded hollow profiles applications. Despite the studied cross-sections are not good enough under axial loads, 3D printing allows complex geometries and exploring more sophisticated cross-sections that could lead to higher axial *SEA* values.

Acknowledgments

Authors thank the Ministry of Science and Innovation, Spain through project ADDICOMP (grant RTI2018-094435-B-C33), the Basque Government (IT883-16, PI2017-49) and the Gipuzkoako Foru Aldundia (Exp. 91/17) for the provided financial support.

References

[1] Friedrich K, Almajid AA. Manufacturing Aspects of Advanced Polymer Composites for Automotive Applications. Appl Compos Mater 2013;20:107–28. https://doi.org/10.1007/s10443-012-9258-7.

[2] Reynolds N, Balan Ramamohan A. High-Volume Thermoplastic Composite Technology for Automotive Structures. Adv Compos Mater Automot Appl 2013:29–50. https://doi.org/doi:10.1002/9781118535288.ch2.

[3] Saenz-Dominguez I, Tena I, Esnaola A, Sarrionandia M, Torre J, Aurrekoetxea J. Design and characterisation of cellular composite structures for automotive crash-boxes manufactured by out of die ultraviolet cured pultrusion. Compos Part B Eng 2019;160:217–24. https://doi.org/10.1016/j.compositesb.2018.10.046.

[4] Tena I, Esnaola A, Sarrionandia M, Ulacia I, Torre J, Aurrekoetxea J. Out of die ultraviolet cured pultrusion for automotive crash structures. Compos Part B Eng 2015;79:209–16. https://doi.org/10.1016/j.compositesb.2015.04.044.

[5] Heimbs S, Strobl F, Middendorf P. Integration of a composite crash absorber in aircraft fuselage vertical struts. Int J Veh Struct Syst 2011;3:87–95. https://doi.org/10.4273/ijvss.3.2.03.

[6] Rouzegar J, Assaee H, Niknejad A, Elahi SA. Geometrical discontinuities effects on lateral crushing and energy absorption of tubular structures. Mater Des 2015;65:343–59. https://doi.org/10.1016/j.matdes.2014.09.041.

[7] Belingardi G, Beyene AT, Koricho EG. Geometrical optimization of bumper beam profile made of pultruded composite by numerical simulation. Compos Struct 2013;102:217–25. https://doi.org/10.1016/j.compstruct.2013.02.013.

[8] Abdewi EF, Sulaiman S, Hamouda AMS, Mahdi E. Quasi-static axial and lateral crushing of radial corrugated composite tubes. Thin-Walled Struct 2008;46:320–32. https://doi.org/10.1016/j.tws.2007.07.018.

[9] Esnaola A, Tena I, Saenz-Dominguez I, Aurrekoetxea J, Gallego I, Ulacia I. Effect of the manufacturing process on the energy absorption capability of GFRP crush structures. Compos Struct 2018;187:316–324. https://doi.org/10.1016/j.compstruct.2017.12.079.

[10] Esnaola A, Tena I, Aurrekoetxea J, Gallego I, Ulacia I. Effect of fibre volume fraction on energy absorption capabilities of E-glass/polyester automotive crash structures. Compos Part B Eng 2016;85:1–7. https://doi.org/10.1016/j.compositesb.2015.09.007.

[11] Ma Y, Jin S, Zhang S. Effect of trigger on crashworthiness of unidirectional carbon fibre reinforced polyamide 6 composites. Plast Rubber Compos 2018;47:208–20. https://doi.org/10.1080/14658011.2018.1466502.

[12] Hamada H, Coppola JC, Hull D, Maekawa Z, Sato H. Comparison of energy absorption of carbon/epoxy and carbon/PEEK composite tubes. Composites 1992;23:245–52. https://doi.org/10.1016/0010-4361(92)90184-V.

[13] Agirregomezkorta A, Martínez AB, Sánchez-Soto M, Aretxaga G, Sarrionandia M, Aurrekoetxea J. Impact behaviour of carbon fibre reinforced epoxy and non-isothermal cyclic butylene terephthalate composites manufactured by vacuum infusion. Compos Part B Eng 2012;43:2249–56. https://doi.org/10.1016/j.compositesb.2012.01.091.

[14] Trudel-Boucher D, Champagne M.F. Stamping of high performance thermoplastic composite intrusion beams. IOP Conference Series Materials Science and Engineering 418(1):012127. https://doi.org/ 10.1088/1757-899X/418/1/012127

[15] Frketic J, Dickens T, Ramakrishnan S. Automated manufacturing and processing of fiber-reinforced polymer (FRP) composites: An additive review of contemporary and modern techniques for advanced materials manufacturing. Addit Manuf 2017;14:69–86. https://doi.org/10.1016/j.addma.2017.01.003.

[16] González C, Vilatela JJ, Molina-Aldareguía JM, Lopes CS, LLorca J. Structural composites for multifunctional applications: Current challenges and future trends. Prog Mater Sci 2017;89:194–251. https://doi.org/10.1016/j.pmatsci.2017.04.005.

[17] Kabir SMF, Mathur K, Seyam AFM. A critical review on 3D printed continuous fiber-reinforced composites: History, mechanism, materials and properties. Compos Struct 2020;232. https://doi.org/10.1016/j.compstruct.2019.111476.
[18] Parandoush P, Lin D. A review on additive manufacturing of polymer-fiber composites. Compos Struct 2017;182:36–53. https://doi.org/10.1016/j.compstruct.2017.08.088.
[19] Wang X, Jiang M, Zhou Z, Gou J, Hui D. 3D printing of polymer matrix composites: A review and prospective. Compos Part B Eng 2017;110:442–58. https://doi.org/10.1016/j.compositesb.2016.11.034.
[20] Yang C, Tian X, Liu T, Cao Y, Li D. 3D printing for continuous fiber reinforced thermoplastic composites: Mechanism and performance. Rapid Prototyp J 2017;23:209–15. https://doi.org/10.1108/RPJ-08-2015-0098.
[21] Matsuzaki R, Ueda M, Namiki M, Jeong TK, Asahara H, Horiguchi K, et al. Three-dimensional printing of continuous-fiber composites by in-nozzle impregnation. Sci Rep 2016;6. https://doi.org/10.1038/srep23058.
[22] Liu T, Tian X, Zhang M, Abliz D, Li D, Ziegmann G. Interfacial performance and fracture patterns of 3D printed continuous carbon fiber with sizing reinforced PA6 composites. Compos Part A Appl Sci Manuf 2018;114:368–76. https://doi.org/10.1016/j.compositesa.2018.09.001.
[23] Goh GD, Dikshit V, Nagalingam AP, Goh GL, Agarwala S, Sing SL, et al. Characterization of mechanical properties and fracture mode of additively manufactured carbon fiber and glass fiber reinforced thermoplastics. Mater Des 2018;137:79–89. https://doi.org/10.1016/j.matdes.2017.10.021.
[24] Justo J, Távara L, García-Guzmán L, París F. Characterization of 3D printed long fibre reinforced composites. Compos Struct 2018;185:537–48. https://doi.org/10.1016/j.compstruct.2017.11.052.
[25] Caminero MA, Chacón JM, García-Moreno I, Reverte JM. Interlaminar bonding performance of 3D printed continuous fibre reinforced thermoplastic composites using fused deposition modelling. Polym Test 2018;68:415–23. https://doi.org/10.1016/j.polymertesting.2018.04.038.
[26] Caminero MA, Chacón JM, García-Moreno I, Rodríguez GP. Impact damage resistance of 3D printed continuous fibre reinforced thermoplastic composites using fused deposition modelling. Compos Part B Eng 2018;148:93–103. https://doi.org/10.1016/j.compositesb.2018.04.054.
[27] Araya-Calvo M, López-Gómez I, Chamberlain-Simon N, León-Salazar JL, Guillén-Girón T, Corrales-Cordero JS, et al. Evaluation of compressive and flexural properties of continuous fiber fabrication additive manufacturing technology. Addit Manuf 2018;22:157–64. https://doi.org/10.1016/j.addma.2018.05.007.
[28] Iragi M, Pascual-González C, Esnaola A, Lopes CS, Aretxabaleta L. Ply and interlaminar behaviours of 3D printed continuous carbon fibre-reinforced thermoplastic laminates; effects of processing conditions and microstructure. Addit Manuf 2019;30. https://doi.org/10.1016/j.addma.2019.100884.
[29] J.M. Chacón, M.A. Caminero, P.J. Núñez, E. García-Plaza, I. García-Moreno, J.M. Reverte. Additive manufacturing of continuous fibre reinforced thermoplastic composites using fused deposition modelling: Effect of process parameters on mechanical properties. Composites Science and Technology 181, 2019. 10.1016/j.compscitech.2019.107688
[30] Blok LG, Longana ML, Yu H, Woods BKS. An investigation into 3D printing of fibre reinforced thermoplastic composites. Addit Manuf 2018;22:176–86. https://doi.org/10.1016/j.addma.2018.04.039.
[31] Tsouknidas A, Pantazopoulos M, Katsoulis I, Fasnakis D, Maropoulos S, Michailidis N. Impact absorption capacity of 3D-printed components fabricated by fused deposition modelling. Mater Des 2016;102:41–4. https://doi.org/10.1016/j.matdes.2016.03.154.
[32] Pollard D, Ward C, Herrmann G, Etches J. The manufacture of honeycomb cores using Fused Deposition Modeling. Adv Manuf Polym Compos Sci 2017;3:21–31. https://doi.org/10.1080/20550340.2017.1306337.
[33] Bates SRG, Farrow IR, Trask RS. 3D printed polyurethane honeycombs for repeated tailored energy absorption. Mater Des 2016;112:172–83. https://doi.org/10.1016/j.matdes.2016.08.062.

[34] Sugiyama K, Matsuzaki R, Ueda M, Todoroki A, Hirano Y. 3D printing of composite sandwich structures using continuous carbon fiber and fiber tension. Compos Part A Appl Sci Manuf 2018;113:114–21. https://doi.org/10.1016/j.compositesa.2018.07.029.
[35] Hou Z, Tian X, Zhang J, Li D. 3D printed continuous fibre reinforced composite corrugated structure. Compos Struct 2018;184:1005–10. https://doi.org/10.1016/j.compstruct.2017.10.080.
[36] Hou S, Li T, Jia Z, Wang L. Mechanical properties of sandwich composites with 3d-printed auxetic and non-auxetic lattice cores under low velocity impact. Mater Des 2018;160:1305–21. https://doi.org/10.1016/j.matdes.2018.11.002.
[37] Li T, Wang L. Bending behavior of sandwich composite structures with tunable 3D-printed core materials. Compos Struct 2017;175:46–57. https://doi.org/10.1016/j.compstruct.2017.05.001.
[38] Pascual-González C, Iragi M, Fernández A, Fernández-Blázquez JP, Aretxabaleta L, Lopes CS. An approach to analyse the factors behind the micromechanical response of 3D-printed composites. Compos Part B Eng 2020;186. https://doi.org/10.1016/j.compositesb.2020.107820.
[39] Matsuzaki R, Nakamura T, Sugiyama K, Ueda M, Todoroki A, Hirano Y, et al. Effects of Set Curvature and Fiber Bundle Size on the Printed Radius of Curvature by a Continuous Carbon Fiber Composite 3D Printer. Addit Manuf 2018;24:93–102. https://doi.org/10.1016/j.addma.2018.09.019.
[40] Mamalis AG, Manolakos DE, Ioannidis MB, Papapostolou DP. On the response of thin-walled CFRP composite tubular components subjected to static and dynamic axial compressive loading: Experimental. Compos Struct 2005;69:407–20. https://doi.org/10.1016/j.compstruct.2004.07.021.

Vitae

Mechanical Engineer graduated from UPV/EHU Engineering Technical School (University of Basque Country) in 2006. He has been working during ten years in TECNALIA RESEARCH AND INNOVATION (Basque Country R&D centre). Since 2017, he is a PhD student at the research group of Polymer and Composites Technology at Mondragon Unibertsitatea. His research is focused on Design and Optimization of 3D printed composite structures, developing lightweighting solutions and impact loading applications. He actually is involved in different fundamental research projects such as European projects or industrial transfer projects oriented to the automotive industry and mechanical engineering equipments.

Table 1. Tensile test properties of printed composite materials. [28,38].

Material	Density (g/cm^3)	Modulus Elasticity (GPa)	Tensile Strength (MPa)	Break strain (%)
Onyx®	1.18	1.4	36	58
CF-PA	1.4	54	700	1.5

Table 2. Transverse section's geometrical properties.

Profile	Area (mm^2)	I_{yy} (mm^4)
Fold	333.6	45656
Hexagonal	336.7	49513

Table 3. Extrusion and filling parameters of the printing process.

Extrusion parameter	Value		Filling parameter	Value	
Material	Onyx®	CF-PA	Filling pattern	Isotropic	Concentric
Layer thickness (mm)	0.125		Number of floor/roof layer	2	2
Nozzle diameter (mm)	0.4	0.9	Number of wall contours	1	1
Temperature (ºC)	273	252	Concentric Fibre Rings	0	2
Printing speed (mm/s)	15		Fibre Angles - Walls to Reinforce	0º	All walls

Table 4. Static axial compression test results.

Test specimen	**Mean Load** P_{mean} (kN)	**Max Load** P_{max} (kN)	**Load Uniformity** LU (%)	**Stroke Efficiency** *SE* (%)	**Specimen Mass** m_t (g)	**Specific Energy** *SEA* (kJ/kg)	**Failure Mode** (-)
FLA	21.4 (±0.5)	48.5 (±3.8)	44	22	26	11.8 (±0.8)	Unstable
FCA	12.6 (±0.1)	22.2 (±0.6)	57	76	24	23.9 (±1.0)	Stable
HLA	13.3 (±1.0)	34.3 (±1.6)	34	25	26	10.6 (±0.8)	Unstable
HCA	12.2 (±1.5)	25.5 (±1.0)	48	73	24	22.2 (±2.0)	Stable

Table 5. Static radial compression test results.

Test specimen	**Mean Load** P_{mean} (kN)	**Max Load** P_{max} (kN)	**Load Uniformity** LU (%)	**Stroke Efficiency** *SE* (%)	**Specimen Mass** m_t (g)	**Specific Energy** *SEA* (kJ/kg)	**Failure Mode** (-)
FLR	0.9 (±0.1)	3.5 (±1.5)	30	45	26	0.6 (±0.2)	Stable
FCR	6.3 (±0.6)	15.8 (±1.2)	40	64	24	5.9 (±0.6)	Stable
HLR	0.2 (±0.1)	0.6 (±0.1)	39	73	26	0.2 (±0.1)	Unstable
HCR	2.0 (±0.1)	0.6 (±0.2)	32	54	24	1.6 (±0.1)	Unstable

Table 6. Summary of 3D printed profiles with stable (✓) and unstable (×) crush behaviour.

	Axial		Radial	
	Longitudinal	Concentric	Longitudinal	Concentric
Fold	×	✓	✓	✓
Hexagonal	×	✓	×	×

Table 7. *SEA* values for axial loading.

Material	**Manufacturing process**	**Section shape**	***SEA* (kJ/kg)**	**% vol. fibre**	**Reference**
GF-Vinyl ester	Pultrusion (0º)	Hexagonal	64	52	[3]
CF-Epoxy	Autoclave (±45º)	Tubular	53	55	[12]

Table 8. *SEA* values for radial loading.

Material	**Manufacturing process**	**Section shape**	***SEA* (kJ/kg)**	**% vol. fibre**	**Reference**
GF-Vinylester	Hand Lay-up (±30º)	Tubular	2.5	-	[6]
GF-Epoxy	Filament Winding	Tubular	0.3	-	[8]

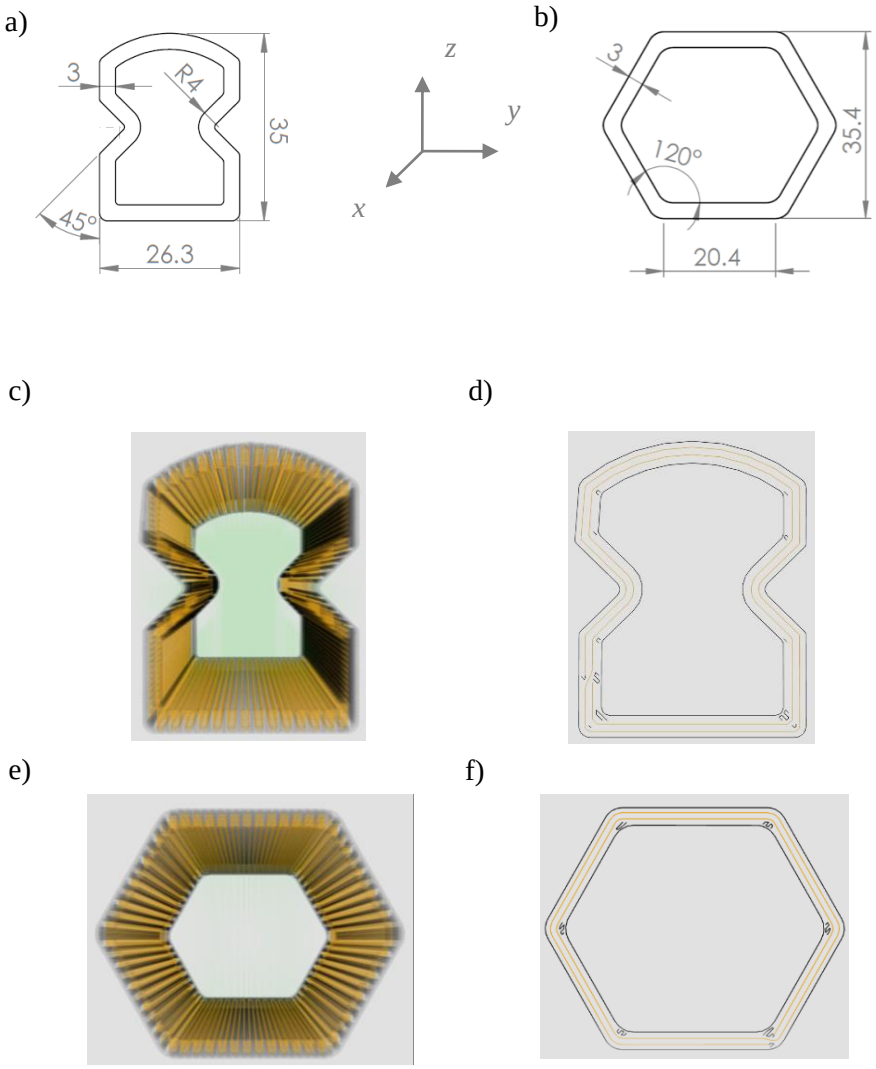

Figure 1. a) Profile geometry Fold [7] and Hexagonal (b) [3,9,10].
c) Longitudinal and d) Concentric printing patten for Fold.
e) Longitudinal and f) Concentrical printing pattern (exported imagens from Eiger©).
All measurements are in mm. X-axis corresponds with Longitudinal axis of the profile.

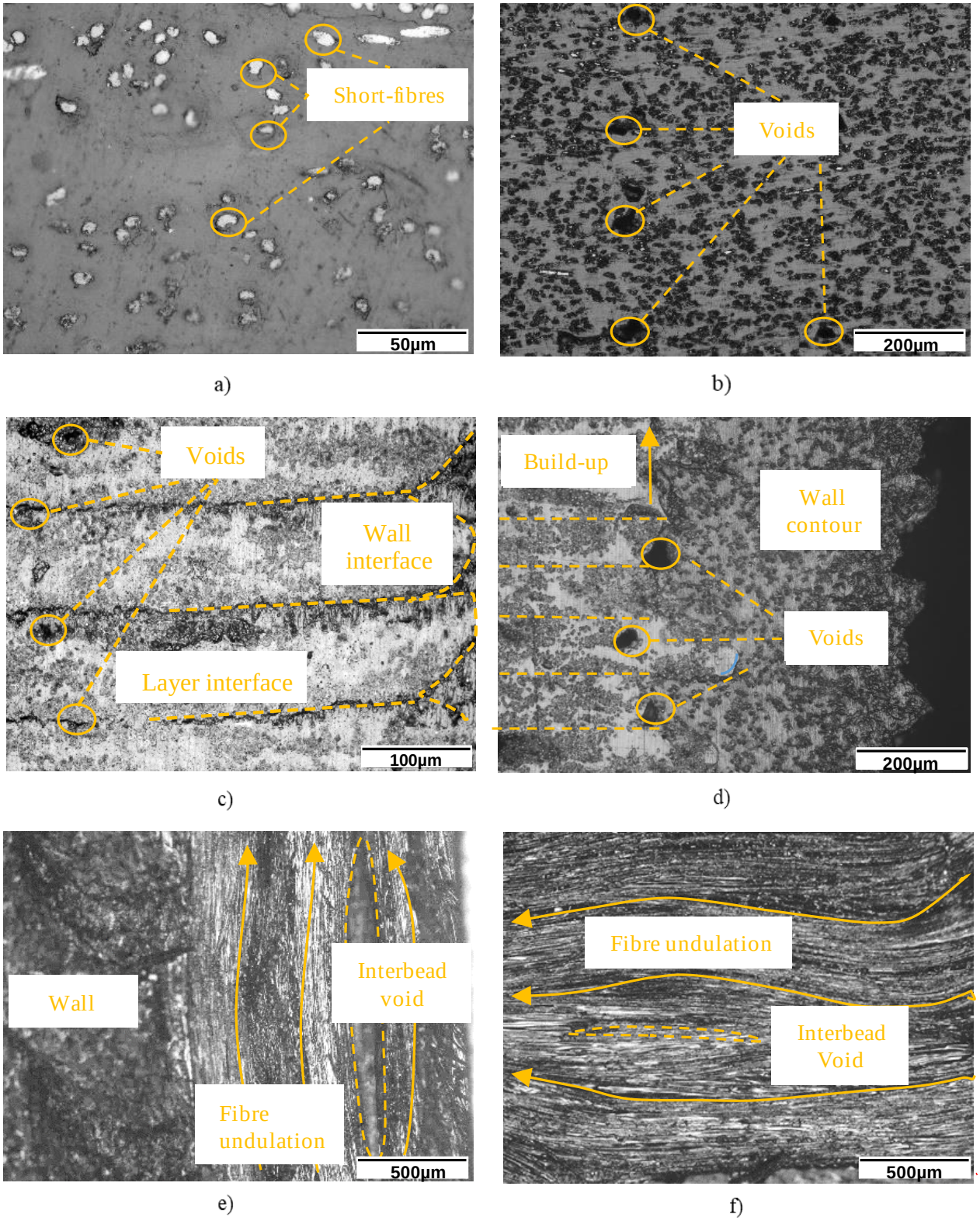

Figure 2. Printing quality and interface aspect of materials as printed. Onyx® contour wall material: a) Short-fibres and b) Interbead voids – Fold mid-span. Longitudinal samples: c) Layer and contour interface aspect and voids, d) Layer-by-layer build-up and resin-rich zones - Fold upper corner and e) Fibres undulation and interbead void – Fold corrugation. Concentric sample: f) Fibres ring undulation including straight printing paths. - Hexagonal bottom edge.

Color should be used for figure 2 in print

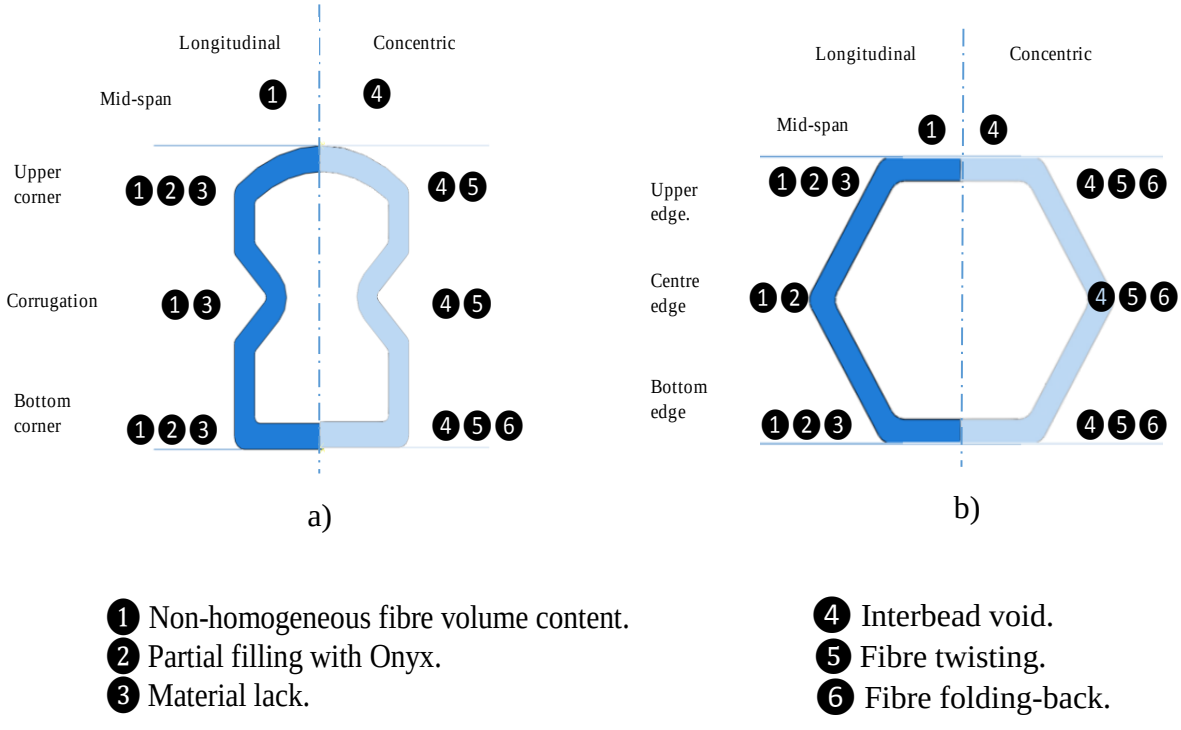

Figure 3. Fibre-placement defects at singular points for Longitudinal and Concentric samples. a) Fold and b) Hexagonal profiles.

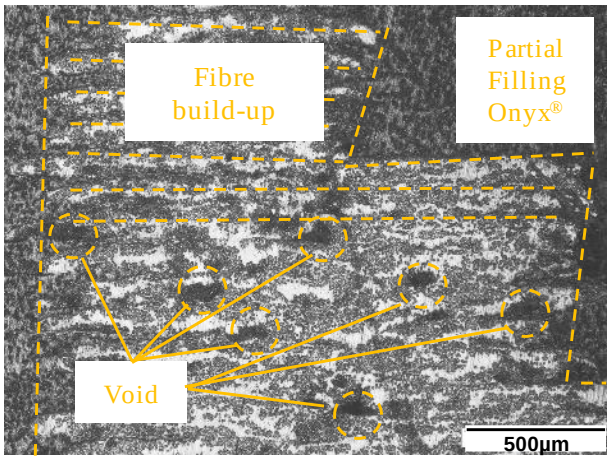

a)

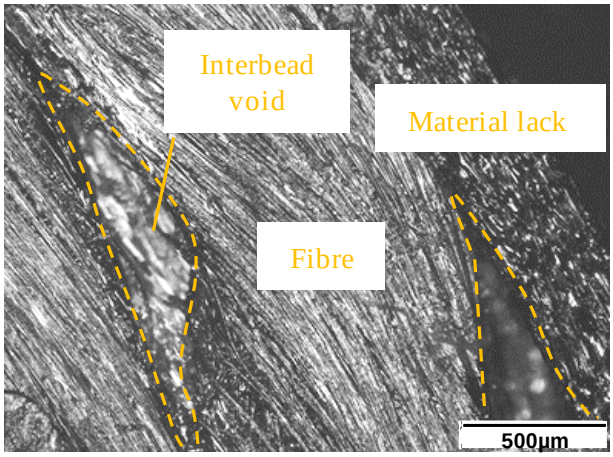

d)

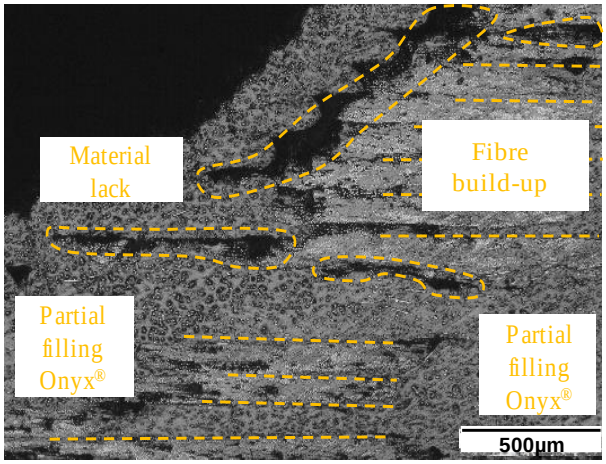

b)

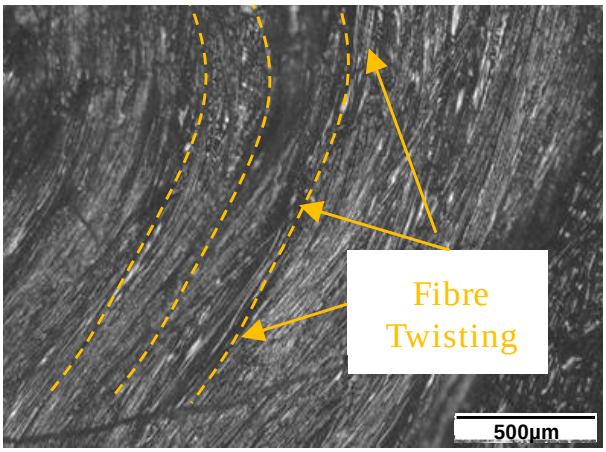

e)

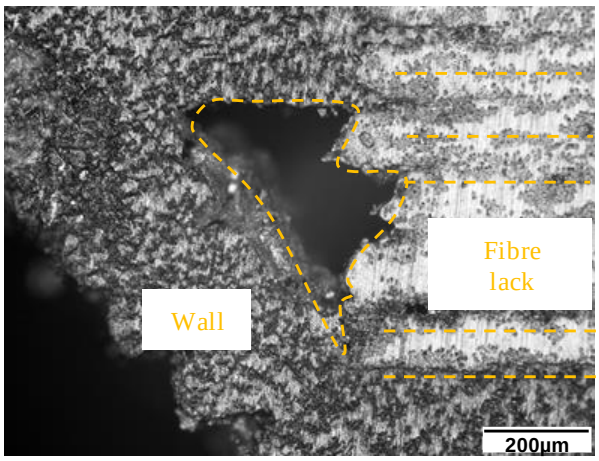

c)

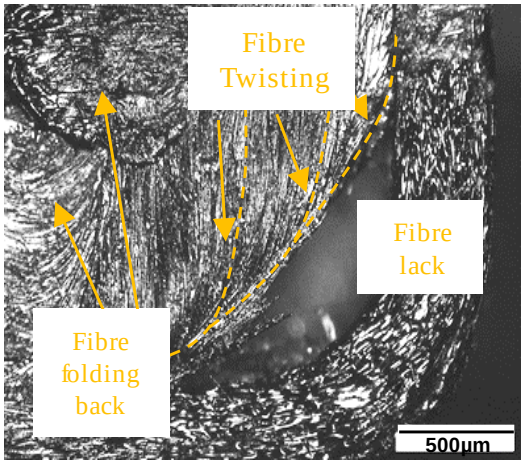

f)

Figure 4. Fibre placement defects. Longitudinal specimens: a) Non-homogeneous fibre volume content - Fold bottom corner, b) Partial filling with Onyx© and fibre build-up – Hexagonal bottom edge, and c) Material lack - Fold corrugation zone. Concentrical specimens: d) Interbead void – Hexagonal upper edge, e) Fibre twisting – Hexagonal centre edge and f) Fibre folding back – Fold bottom corner.

Color should be used for figure 4 in print

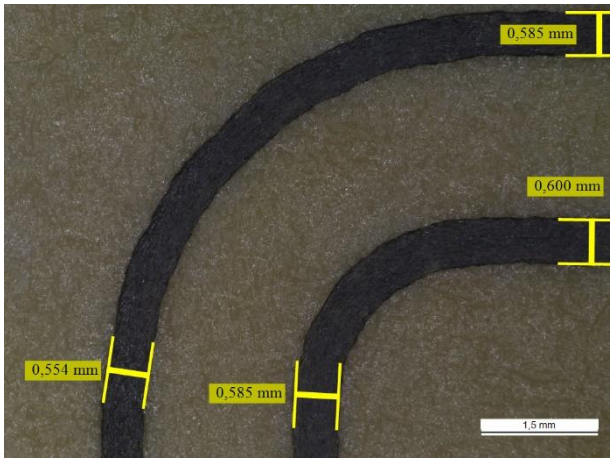

a)

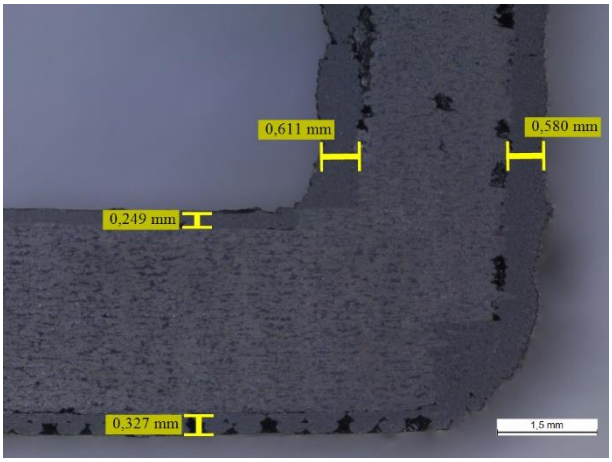

b)

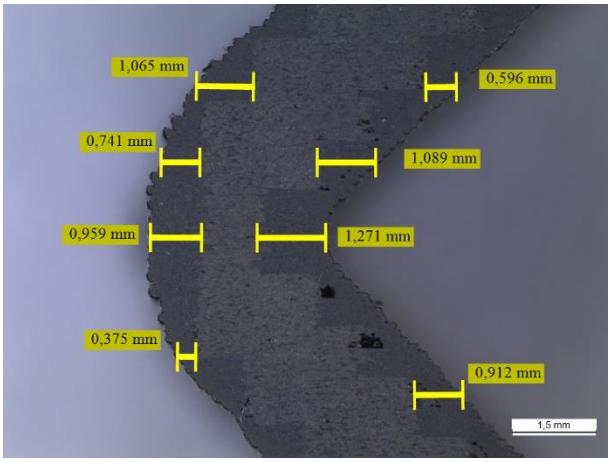

c)

Figure 5. a) Bead width of single bead of Onyx®, b) Transverse cutting plane of longitudinally printed Fold profile at the bottom corner zone and c) at the corrugation.
Color should be used for figure 5 in print

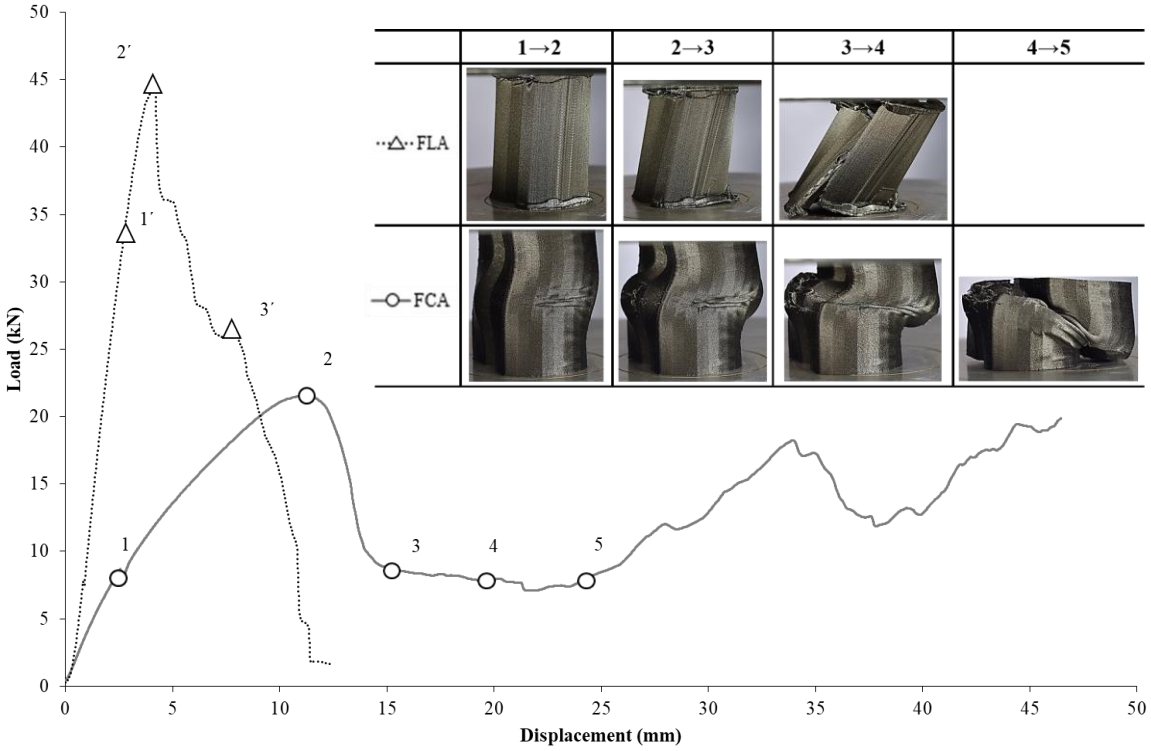

a)

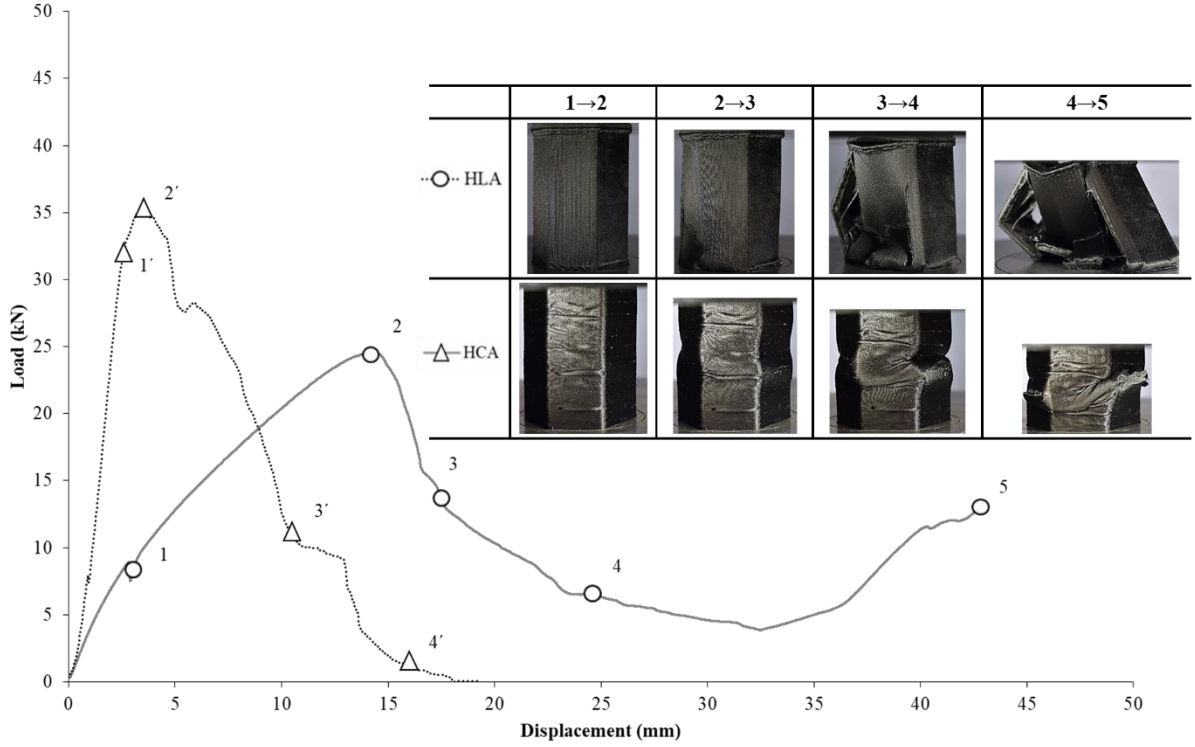

b)

Figure 6. Axial crush curves and patterns for the printed profiles: a) Fold and b) Hexagonal.
Color should be used for figure 6 in print

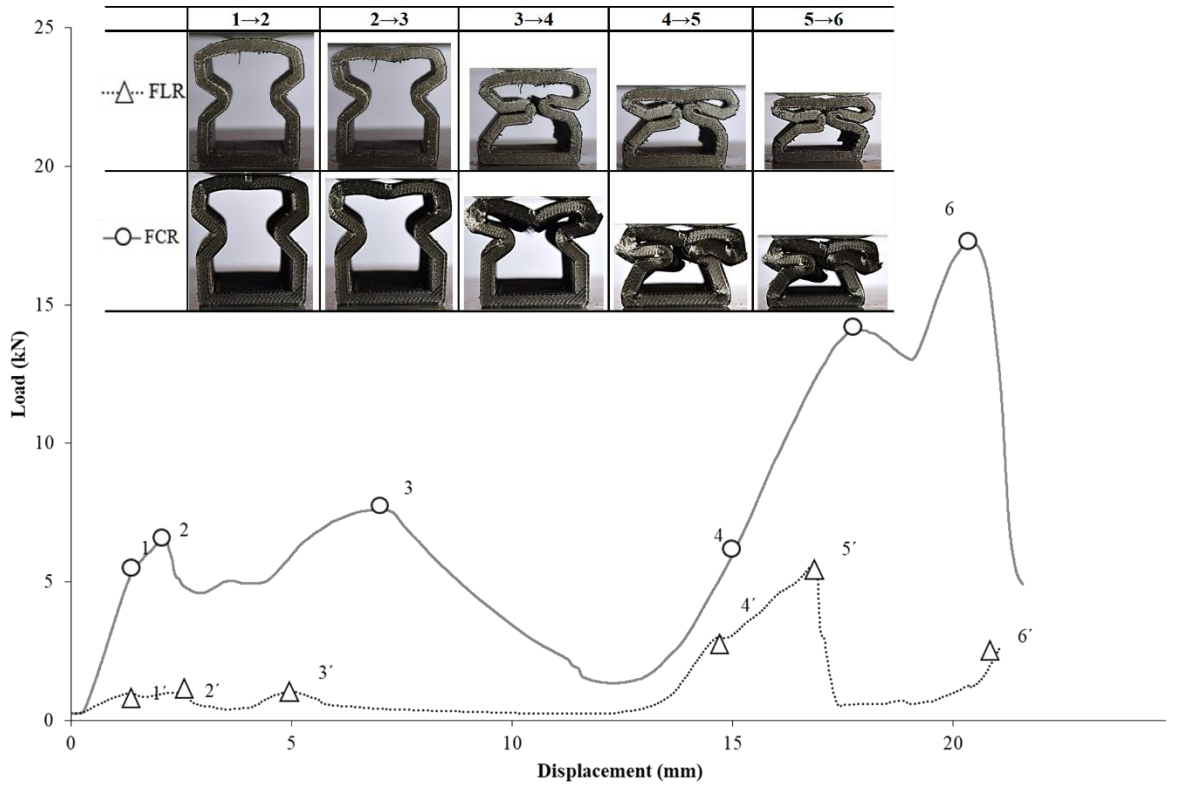

a)

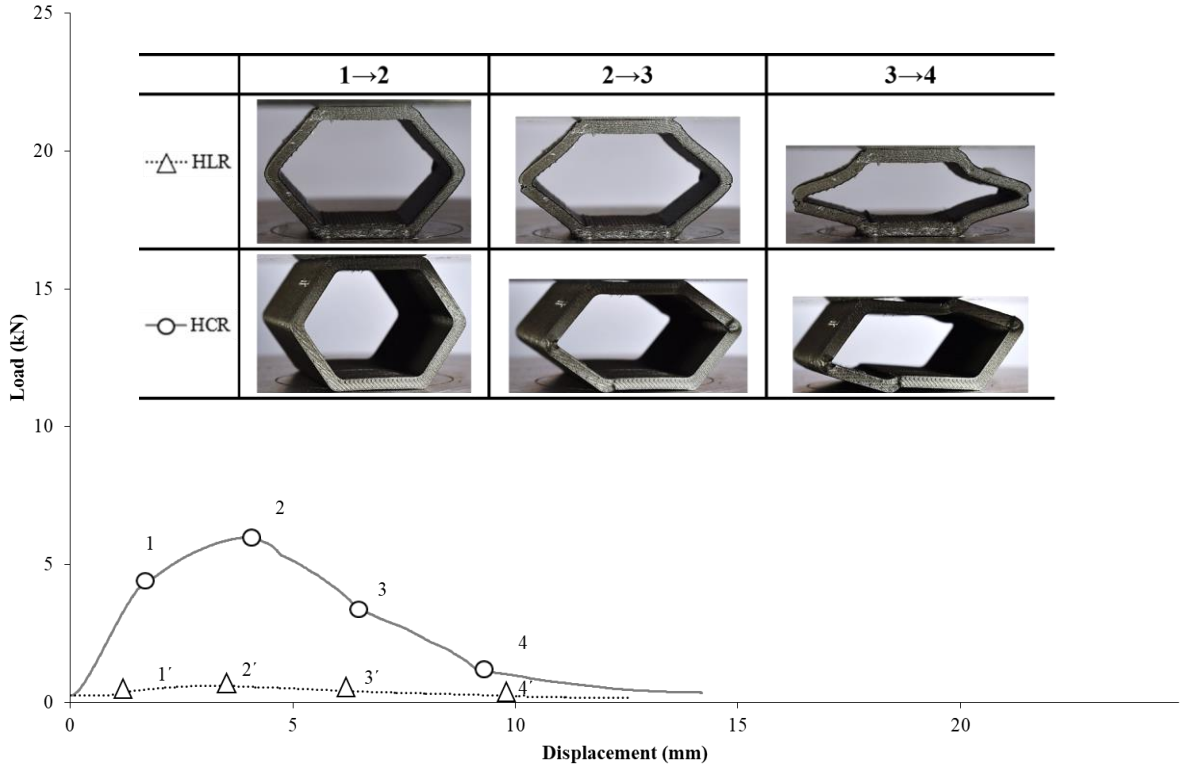

b)

Figure 7. Radial crush curves and patterns for the printed profiles: a) Fold and b) Hexagonal.
Color should be used for figure 7 in print

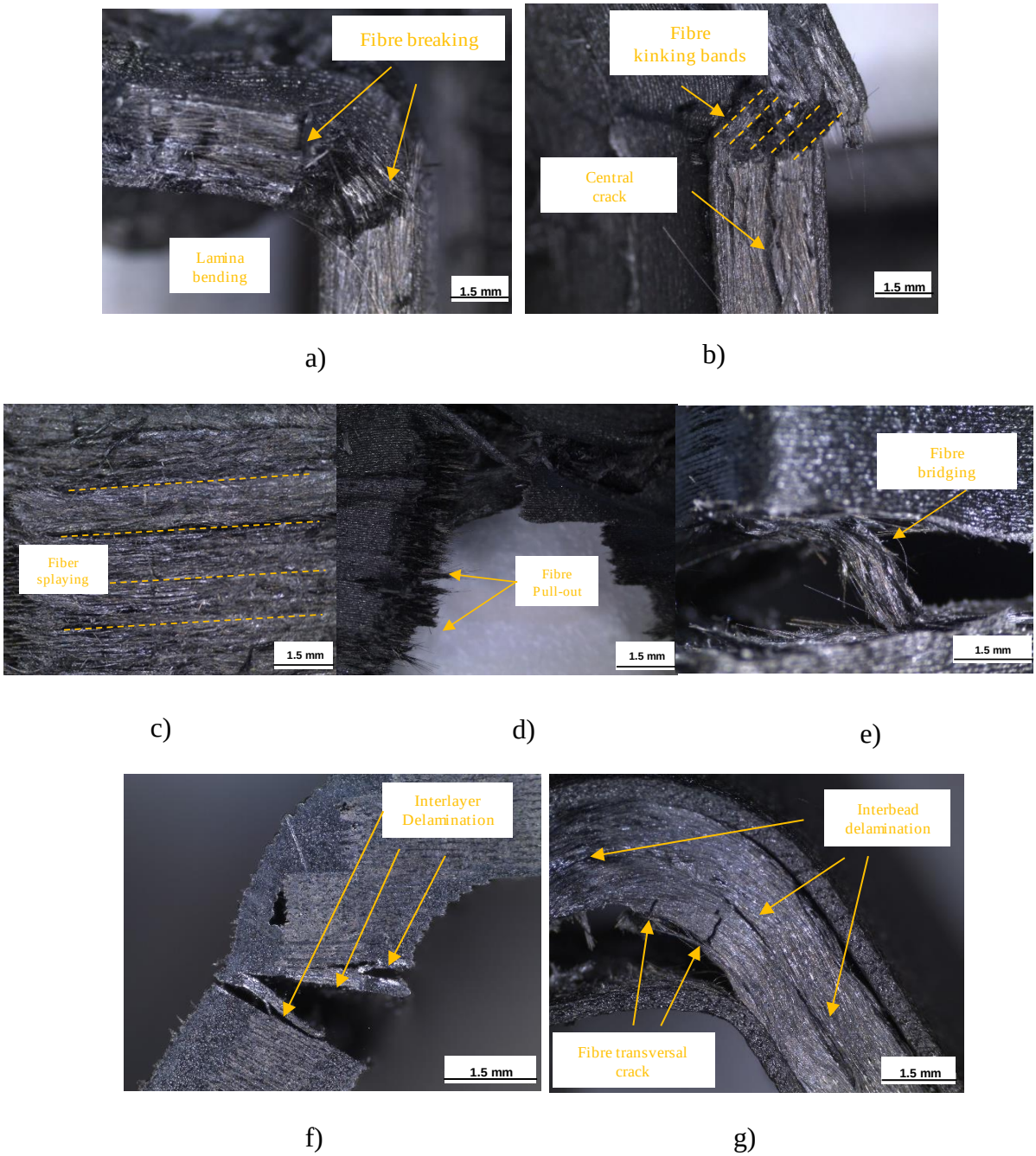

Figure 8. Fracture surface and failure mode: a) Lamina bending of HLA at centre edge, b) Fibre buckling of HLA at centre edge, c) Fibre splaying of FCA, d) Fibre pull-out of FCA, e) Fibre bridging of HCA, f) Interlayer delamination of HLR at upper edge, g) Fibre breaking and interbead delamination of HCR at bottom edge.
Color should be used for figure 8 in print